POLITECNICO DI TORINO
Repository ISTITUZIONALE

Interim results of the H2020 project FITGEN: design and integration of an e-axle for the third-generation electric vehicles

(Article begins on next page)

25 April 2024

Evaluation of Radar Multiple-Scattering Effects from a GPM Perspective. Part I: Model Description and Validation

A. BATTAGLIA

Meteorological Institute, University of Bonn, Bonn, Germany

M. O. AJEWOLE

Department of Physics, Federal University of Technology, Akure, Nigeria

C. SIMMER

Meteorological Institute, University of Bonn, Bonn, Germany

ABSTRACT

A numerical model based on the Monte Carlo solution of the vector radiative transfer equation has been adopted to simulate radar signals. The model accounts for general radar configurations such as airborne/ spaceborne/ground based and monostatic/bistatic and includes the polarization and the antenna pattern as particularly relevant features. Except for contributions from the backscattering enhancement, the model is particularly suitable for evaluating multiple-scattering effects. It has been validated against some analytical methods that provide solutions for the first and second order of scattering of the copolar intensity for pencil-beam/Gaussian antennas in the transmitting/receiving segment. The model has been applied to evaluate the multiple scattering when penetrating inside a uniform hydrometeor layer. In particular, the impact of the phase function, the range-dependent scattering optical thickness, and the effects of the antenna footprint are considered.

1. Introduction

The precipitation radar (PR) at 13.8 GHz on the Tropical Rainfall Measuring Mission (TRMM) satellite has played a very significant role in the characterization of clouds and precipitation particles aloft (Kummerow et al. 1998; Kozu et al. 2001). Future spaceborne radars are envisaged to operate at higher frequencies such as 35.5 GHz for the radar planned for the Global Precipitation Measurement (GPM) satellite and its European version (EGPM; Mugnai 2003). The "CloudSat" radar at 94 GHz is already deployed to investigate the vertical structure of clouds (Stephens et al. 2002).

The interpretation of radar scans is always made on the assumption of negligible multiple-scattering (MS) effects. However, as the frequency of operations of the

PR is raised, some factors may come into play that have the potential to enhance the significance of higher order of scattering in the radar echo. Among such factors are the increase in the optical thickness of the medium, the decrease of the mean free path of radiation (defined as the inverse of the extinction coefficient) toward values comparable to or smaller than the radar footprint dimension, the increase of scattering versus absorption cross sections [e.g., for raindrops see Fig. 3.6 in Gasiewski (1993)], and the modification of hydrometeor scattering-phase functions, which become more peaked in the forward direction. This factor is highlighted by the increase of the asymmetry parameter g [e.g., Fig. 3.7 in Gasiewski (1993) and center-left panels in Figs. 5 and 7–9 of Battaglia et al. (2006), hereinafter referred to as Part II]. Because previous studies such as Ito et al. (1995), Marzano et al. (2003), Kobayashi et al. (2004, 2005), and Battaglia et al. (2005a) showed that the borderline of relevance for MS effects lies between the new-generation spaceborne radars (at K_a and K_u band) and the TRMM PR at X band (see Kozu et al.

Corresponding author address: Alessandro Battaglia, Meteorological Institute, University of Bonn, Auf dem Hugel, 20, 53121 Bonn, Germany.
E-mail: batta@uni-bonn.de

2001), a detailed investigation of the problem of MS at frequencies in the millimeter region is a timely endeavor.

The MS phenomenon in active remote sensing has been well studied within the lidar community (see Bissonnette et al. 1995; Bissonnette 1996, and references therein). In typical lidar configuration, this phenomenon is enhanced by the higher optical thickness and higher single-scattering (SS) albedos typical for visible and near-infrared regions. Because of the small horizontal footprint of lidar systems (fields of view are within 0.1–5 mrad), the MS effect is enhanced by the strongly peaked phase function that is characteristic of ice/water particles in the optical-scattering regime. This property allows the analysis to focus on scattering in the forward direction only and to derive a closed form of the MS lidar equation (Bissonnette 1996).

When radar systems are used for active remote sensing of precipitation, it is observed that very few studies on MS effects have been carried out (Hubbert and Bringi 2000; Oguchi et al. 1994; Ito et al. 1995; Marzano et al. 2003; Kobayashi et al. 2005). Hubbert and Bringi (2000) developed a three-body scatter model to explain flare echoes or "hail spikes," which are special signatures in reflectivity and differential reflectivity observed at S-band and C-band signals in hailstorms. The numerical model is restricted to three-body scatter, and it cannot be extended to general MS theory. A similar model aimed at validating the second order of scattering has been developed in our general MS model (section 4b). Note also that the mirror-image return, frequently observed in most of the TRMM PR profiles over ocean (e.g., Olson et al. 2001), is based on an MS mechanism that involves surface, rain, and then surface.

Oguchi et al. (1994) and Marzano et al. (2003) evaluated MS effects and their impact on rainfall-rate estimates. These studies concluded that MS signals are significant, especially in heavy-rain cases. In particular, Marzano et al. (2003) showed that, in the presence of strongly attenuating media, MS contributions will enhance the detection of rain by partly overcoming the apparent path attenuation. This effect has an immediate impact on rainfall retrieval algorithms (e.g., Testud et al. 1992; Marzoug and Amayenc 1994; Iguchi et al. 2000). In fact, the correction of attenuation is important in spaceborne monitoring of rainfall for which the frequencies used are higher but the path through the rain is fairly short. The studies by Oguchi et al. (1994) and Marzano et al. (2003), however, did not explicitly account for the effect of the antenna pattern and of the backscattering enhancement on radiation undergoing MS. In contrast to these theoretical studies that considered infinitely extended plane waves (which assump-

tion overestimates the MS effect, as will be shown later in this study), more recent studies have taken into account the antenna pattern effect. In the study by Kobayashi et al. (2004, 2005), reductions in MS effects were derived by considering spherical waves with a Gaussian antenna pattern, including depolarizing effects. Their conclusion can be summarized as follows. The differences from the plane-wave results are not significant when the optical thickness is small. However, when the latter increases, the differences become significant and essentially depend on the ratio of radar footprint radius to the mean free path of hydrometeors. In this regime, for a radar footprint that is smaller than the mean free path, the MS (inclusive of the backscattering enhancement) in reflectivity corresponding to spherical waves is significantly less pronounced than in the case of the plane-wave theory. Whereas the theory of Kobayashi et al. (2005) treats a uniform single-layered cloud illuminated by continuous waves, Battaglia et al. (2005a) simulated the MS for random media in multiple cloud layers with pulsed radars. The findings by Kobayashi et al. (2004, 2005) were confirmed in Battaglia et al. (2005a) in which the reduction in MS due to illumination by a finite beamwidth is demonstrated for a PR down-looking configuration for heavy convective rain. In particular, it was shown how the MS effect vanishes when passing from a typical PR footprint diameter (on the order of 4–5 km) to very high resolution airborne systems (on the order of hundreds of meters) at 35 GHz. As a conclusion from these results, infinitely extended plane-wave computations can be used only to pinpoint when MS is negligible; when MS effects are relevant, this kind of computation is accurate only when the radar footprint radius is much larger than the mean free path.

In this two-part series of papers, attention is focused on the two frequencies to be used in the planned GPM core satellite: 13.8 and 35.5 GHz. First, a general insight into MS effects is given by discussing the impacts of the different factors involved in the problem (e.g., scattering properties, radar configuration, or antenna pattern). Then, in Part II estimates of the MS effects at the two GPM frequencies are provided when using both the configurations of the envisaged spaceborne radars and those set up in preliminary airborne campaigns.

In this first part, a numerical Monte Carlo (MC) model suitable for a pulsed active-sensor MS evaluation is described and validated. In section 2, the radar equation, which is extended to account for MS contributions, is briefly reviewed. Section 3 describes the MC code developed to evaluate the MS effect in radar echoes. Using the model, the results obtained for

the first and second order of scattering are validated in section 4. In section 5, the model is applied to a uniform homogeneous layer to explain the general features of the MS signal. Conclusions are drawn in section 6.

2. The radar equation in the presence of multiple scattering

The classical radar equation (e.g., Doviak and Zrnić 1984; Bringi and Chandrasekar 2001) usually provides the apparent reflectivity as a function of SS contributions only. Taking an approach similar to that adopted by Marzano et al. (2003), how to generalize the radar equation to include MS components is briefly summarized. Here emphasis is on antenna-related quantities because of their importance in the following developments.

The apparent (or effectively measured) received power due to the range gate at distance r in the presence of MS (higher than the SS contributions) can be generally expressed (Tsang et al. 1985) as

$$\langle P_{aR}(r) \rangle = A_{e0} \int_{4\pi} F_n(\hat{\Omega}) \langle I_a(r, \hat{\Omega}) \rangle \, d\Omega$$
$$= \frac{\lambda^2}{4\pi} \int_{4\pi} G(\hat{\Omega}) \langle I_a(r, \hat{\Omega}) \rangle \, d\Omega, \qquad (1)$$

with $\langle I_a(r, \hat{\Omega}) \rangle$ being the mean value of the apparent received specific intensity. Here, $F_n(\hat{\Omega})$ is the normalized (in the sense that the maximum is equal to 1) antenna pattern (equal to the square of the modulus of the antenna field pattern); $G(\hat{\Omega}) = G_0 F_n(\hat{\Omega})$ is the antenna gain, with $G_0 = (4\pi)/\Omega_p$ being the maximum directive gain and $\Omega_p = \int F_n(\hat{\Omega}) \, d\Omega$ being the antenna pattern solid angle. The maximum antenna equivalent area is $A_{e0} = \lambda^2/(4\pi)G_0$. When only the first order of scattering is retained in the apparent specific intensity, the single- (back-) scattering power is obtained as

$$\langle P_{aR}^{SS}(r) \rangle = A_{e0} \int_{4\pi} F_n(\hat{\Omega}) \langle I_a^{SS}(r, \hat{\Omega}) \rangle \, d\Omega$$
$$= \frac{\lambda^2}{4\pi} \int_{4\pi} G(\hat{\Omega}) \langle I_a^{SS}(r, \hat{\Omega}) \rangle \, d\Omega. \qquad (2)$$

The integral over the solid angle on the right-hand side of Eq. (2) can be simplified under the hypothesis that the SS specific intensity $\langle I_a^{SS}(r, \hat{\Omega}) \rangle$ is constant within the antenna main lobe. This condition is true in particular when dealing with a pencil beam, hereinafter referred to as the SS pencil-beam (SSpb) approximation. When carrying out the integral, Eq. (2) reduces to (Bringi and Chandrasekar 2001)

$$\langle P_{aR}^{SSpb}(r) \rangle = \frac{A_{e0} G_0 \Omega_{2A} \Delta r}{(4\pi)^2} \frac{\pi^5 |K|^2}{\lambda^4} \frac{P_T}{r^2} Z_a^{SSpb}, \qquad (3)$$

where λ is the wavelength, P_T is the transmitted power, Δr is the range resolution, and Z_a^{SSpb} is the SS apparent radar reflectivity at range r and is related to the equivalent reflectivity factor Z_e by

$$Z_a^{SSpb}(r) \equiv Z_e(r) \exp\left[-2 \int_0^r k_{ext}(\xi) \, d\xi \right] = \underbrace{\left[\frac{\lambda^4}{\pi^5 |K|^2} \int_D \sigma_{back}(D) N(D) \, dD \right]}_{Z_e(r)} \underbrace{A_{2\text{-way}}(r)}_{A_{2\text{-way}}(r)}, \qquad (4)$$

with $|K|^2$, σ_{back}, and $N(D)$ being the dielectric factor, the backscattering cross section, and the size distribution of the scatterers contained inside the radar backscattering volume, respectively. In the simulations, the dielectric factor is always normalized to that of water at 0°C (assumed to be equal to 0.93 for all frequencies considered hereinafter). Equation (4) explicitly defines also the two-way attenuation $A_{2\text{-way}}(r)$ at range r.

In Eq. (3), Ω_{2A} is the two-way main-lobe solid angle given by

$$\Omega_{2A} \equiv \int [F_n(\hat{\Omega})]^2 \, d\Omega. \qquad (5)$$

For instance, a Gaussian antenna has an antenna pattern of the form

$$F_n(\eta, \xi) = \exp\left[-4 \log 2 \left(\frac{\eta^2}{\eta_{3dB}^2} + \frac{\xi^2}{\xi_{3dB}^2} \right) \right], \qquad (6)$$

where η and ξ are the angles in the vertical and horizontal antenna planes and (η_{3dB}, ξ_{3dB}) are the respective beamwidths at 3 dB. When the Gaussian antenna is narrow, it follows that

$$\Omega_{2A}^{Gaussian} = \int \int F_n^2(\eta, \xi) \, d\eta \, d\xi \cong \frac{\pi \eta_{3dB} \xi_{3dB}}{8 \log 2}. \qquad (7)$$
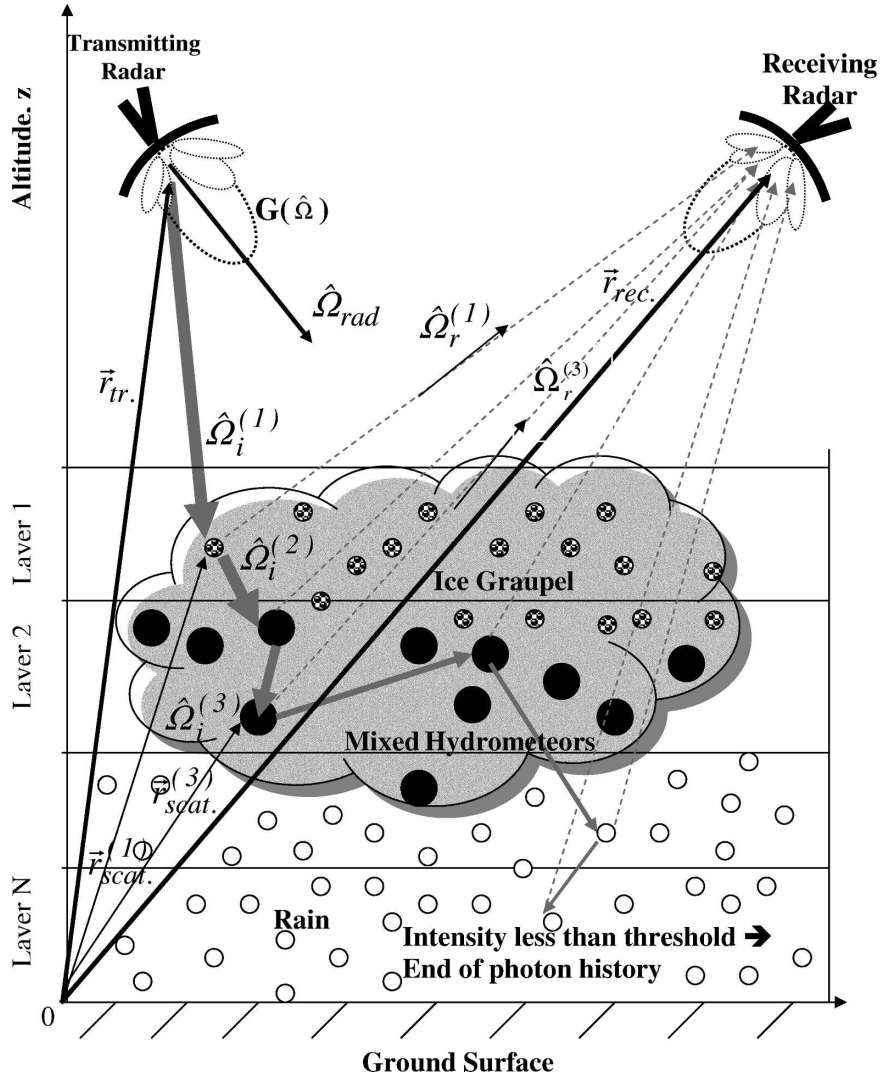
FIG. 1. Geometry and principles of the forward MC algorithm to compute the MS apparent reflectivity Z_a^{MS}.

By comparing Eqs. (1) and (3) it is therefore possible to define an apparent MS reflectivity as

$$Z_a^{\mathrm{MS}} \equiv \left[\frac{\displaystyle\int_{4\pi} F_n(\hat{\mathbf{\Omega}})\langle I_a(r, \hat{\mathbf{\Omega}})\rangle r^2 \, d\Omega}{P_T} \right] \frac{\lambda^4}{\pi^5 |K|^2} \frac{(4\pi)^2}{G_0 \Omega_{2A} \Delta r}.$$

(8)

In a similar way, by making use of Eq. (2) Z_a^{SS} ($\leq Z_a^{\mathrm{MS}}$) can be computed by Eq. (8) with the single-scattering contribution I_a^{SS} instead of I_a.

Last, note that Eq. (8) further simplifies to $G_0 \Omega_{2A} = 2\pi$ for a Gaussian antenna pattern and to $G_0 \Omega_{2A} = 4\pi$ for pencil-beam-like antennas.

3. A Monte Carlo approach to simulate the multiple-scattering reflectivity

To compute the apparent MS reflectivity defined by Eq. (8), it is necessary to evaluate the received specific intensity in terms of all relevant scattering orders, as depicted in Fig. 1. To compute Z_a^{MS}, the vector radiative transfer equation has been solved by using a sophisticated MC solution technique (Battaglia et al. 2005b). When reverting to radiative transfer theory, the present MC approach cannot account for the backscattering enhancement phenomenon (see Tsang et al. 1985, chapter 5) because it can only be described adequately by wave theory. For instance, at the second order of scattering the model accounts for the second-order ladder term

only [i.e., the conventional MS term as illustrated in diagram 1b in Kobayashi et al. (2004)] but does not for the second-order cross term [i.e., the contribution from interference of two ray paths mutually satisfying the condition of time-reversal paths as illustrated in diagram 2b in Kobayashi et al. (2004)]. This condition will lead to an underestimation of the MS effect (see Kobayashi et al. 2004, their Fig. 5). However, when considering spaceborne systems, the high-speed platform motion will generally break the right backscattering condition. Conversely, the treatment of scattering order higher than 2 is much easier in our frame.

Instead of using the backward MC technique of Roberti and Kummerow (1999), as done by Marzano et al. (2003), we have modified the forward MC by Battaglia and Mantovani (2005). In the case of an active sensor response simulation, the backward and the forward approaches give identical statistics when the same number of photons is launched. The forward code has, however, the advantage of a complete polarimetric treatment and the capability of accommodating nonisotropic media. Both aspects are crucial for the simulation of radar polarimetric variables. The MC technique was adopted in this study because of its flexibility in simulating both 3D-structured clouds and arbitrary antenna patterns. Because of the 3D nature of the problem as introduced by the presence of the antenna pattern, it is not possible to simplify the radiative transfer equation to a 1D approximation (which has the possibility of analytic and fast codes) as was done by Ferrauto et al. (2004).

The forward MC code by Battaglia and Mantovani (2005) (which was available online at http://www.meteo.uni-bonn.de/mitarbeiter/battaglia/) was developed for passive remote sensing applications. The algorithm has been modified to simulate the active sensor response by keeping track of the distance traveled by each photon and by allowing the radar to be the only source of radiation. As illustrated in Fig. 1, the radar is characterized by

1) a locally transmitting $\mathbf{r}_{tr}$ and receiving position $\mathbf{r}_{rec}$ (to allow for bistatic antenna configurations)—the radar antennas can be positioned at any altitude above, below, or within the cloud, thus allowing for ground-based, spaceborne, and airborne configurations;

2) two pointing angles $\hat{\mathbf{\Omega}}_{rad}^{tr/rec}$ or, equivalent, two angles $(\Theta_{rad}^{tr/rec}, \Phi_{rad}^{tr/rec})$ that correspond to the direction of the main lobe of the transmitting and of the receiving antenna, whose unit vector is expressed as

$$\mathbf{k}_{rad}^{tr/rec} = (\sin\Theta_{rad}^{tr/rec} \cos\Phi_{rad}^{tr/rec}, \sin\Theta_{rad}^{tr/rec}$$
$$\sin\Phi_{rad}^{tr/rec}, \cos\Theta_{rad}^{tr/rec}),$$

with the vertical and horizontal polarization directions being

$$\mathbf{v}_{rad}^{tr/rec} = (\cos\Theta_{rad}^{tr/rec} \cos\Phi_{rad}^{tr/rec}, \cos\Theta_{rad}^{tr/rec} \sin\Phi_{rad}^{tr/rec},$$
$$- \sin\Theta_{rad}^{tr/rec}) \quad \text{and}$$

$$\mathbf{h}_{rad}^{tr/rec} = (-\sin\Phi_{rad}^{tr/rec}, \cos\Phi_{rad}^{tr/rec}, 0);$$

3) two antenna pattern functions $F_n^{tr/rec}(\hat{\mathbf{\Omega}})$ (that can be different in the transmitting and in the receiving segment), typically identified by the two beamwidths defined in Eq. (6);

4) a transmission and a receiving polarization state (like vertical, horizontal, left/right circular polarized); and

5) a range resolution $\Delta r = c\Delta t/2$, with Δt being the pulse duration.

The radar outgoing radiation is simulated by a number N_T of photons per unit time, with N_T high enough to represent the stochastic variability of all processes involved in photon propagation and interactions when released from the transmitting radar antenna with an appropriate polarization state $\bar{\mathbf{I}}^{(0)}(\mathbf{r}_{tr})$ [the Stokes basis is the one defined in Tsang et al. (1985), e.g., for a vertical-polarization transmitting radar $\bar{\mathbf{I}}^{(0)}(\mathbf{r}_{tr}) = (1.0, 0.0, 0.0, 0.0)$]. Note that the overbar indicates the four-dimensional Stokes vector. Each photon is considered to carry a unitary energy (so that N_T corresponds to the total emitted power P_T), and the angular distribution function is that provided by the antenna pattern. For instance, to reproduce the Gaussian pattern of Eq. (6) it is sufficient (House and Avery 1969) to select two uniform random numbers R_1 and R_2 and to define

$$\xi = \sigma_\eta \sqrt{-2.0 \log(R_1)} \cos(2.0\pi R_2) \quad \text{and}$$

$$\eta = \sigma_\xi \sqrt{-2.0 \log(R_1)} \sin(2.0\pi R_2),$$

with $\sigma_\eta = \eta_{3DB}/\sqrt{8\log2}$ and $\sigma_\xi = \xi_{3DB}/\sqrt{8\log2}$, so that ξ and η are Gaussian-distributed random numbers with zero mean and standard deviations equal to σ_η and σ_ξ. The outgoing photon direction can be identified by

$$\hat{\mathbf{\Omega}}_i^{(1)} = a_1 \mathbf{v}_{rad}^{tr} + a_2 \mathbf{h}_{rad}^{tr} + a_3 \mathbf{k}_{rad}^{tr},$$

where $a_1 = x_1/(1 + x_1^2 + x_2^2)^{1/2}$, $a_2 = x_2/(1 + x_1^2 + x_2^2)^{1/2}$, and $a_3 = 1/(1 + x_1^2 + x_2^2)^{1/2}$, with $x_1 = \tan\eta$ and $x_2 = \tan\xi$.

By so doing, all radiance field properties can be computed from statistical properties of the photon density. For instance, when the radiance in a particular direction $\hat{\mathbf{\Omega}}$ at a certain point $\mathbf{r}$ is looked for, it is sufficient to take a surface $\Delta\Sigma$ centered in $\mathbf{r}$ and normal to $\hat{\mathbf{\Omega}}$, and

to count the number of photons n that cross the surface at $\hat{\mathbf{\Omega}}$ within a small solid angle $\Delta\Omega$. The MC stochastic estimation of the radiance will be

$$I(\hat{\mathbf{\Omega}}, \mathbf{r}) = \frac{P_T \sum\limits_{\Delta\Sigma, \Delta\Omega} n(\hat{\mathbf{\Omega}}, \mathbf{r})}{N_T \Delta\Sigma \Delta\Omega} . \qquad (9)$$

In the code, each photon is traced inside the medium: all stochastic processes (distance to collision, probability of scattering, direction of scattered photons, etc.) are simulated as in the MC version for passive sensors and the associated Stokes vectors are properly modified. Biasing techniques are applied to prevent the photons from escaping from the medium and to avoid absorption events (see section 5.2 in Battaglia and Mantovani 2005).

Each time a k-order scattering event occurs at point $\mathbf{r}_{\text{scat}}^{(k)}$, the algorithm computes the contribution to the received intensity. Because we are dealing with an active sensor, this k-order scattering contribution has to be assigned to a range bin. Therefore, the apparent range is computed by adding the total distance traveled by the photon from the transmitting antenna to the interaction point and the distance between the interaction point and the receiver antenna divided by two:

$$\text{range}^{(k)} = 0.5\{\text{dist}[\mathbf{r}_{\text{tr}} \to \mathbf{r}_{\text{scat}}^{(k)}] + |\mathbf{r}_{\text{rec}} - \mathbf{r}_{\text{scat}}^{(k)}|\}.$$

This distance will correspond to a particular range bin encompassing all ranges between $r - \Delta r/2$ and $r + \Delta r/2$. The k-order-of-scattering contribution to the Stokes vector received by the radar for a particular photon (j) will be

$$\bar{\mathbf{I}}_a^{(k)}(r)(j) = F_n^{\text{rec}}[\hat{\mathbf{\Omega}}_v^{(k)}] \, \mathbf{P}_{\text{prop}}[\mathbf{r}_{\text{scat}}^{(k)} \to \mathbf{r}_{\text{rec}}]$$
$$\times \mathbf{S}_{\text{scat}}[\mathbf{r}_{\text{scat}}^{(k)}; \hat{\mathbf{\Omega}}_i^{(k)}, \hat{\mathbf{\Omega}}_v^{(k)}] \, \bar{\mathbf{I}} \, [\mathbf{r}_{\text{scat}}^{(k)}]; \qquad (10)$$

$\mathbf{S}_{\text{scat}}$ represents the normalized phase matrix (see definition in Mishchenko et al. 2000) for the medium at the point $\mathbf{r}_{\text{scat}}^{(k)}$ relative to the incoming direction of the photon before the k-order scattering $\hat{\mathbf{\Omega}}_i^{(k)}$ and to the scattered direction toward the receiving antenna $\hat{\mathbf{\Omega}}_v^{(k)}$ (unit vector corresponding to the vector difference $\mathbf{r}_{\text{rec}} - \mathbf{r}_{\text{scat}}^{(k)}$). It is obvious that, at the first scattering order for monostatic radar, $\hat{\mathbf{\Omega}}_v^{(1)} = -\hat{\mathbf{\Omega}}_i^{(1)}$. In Eq. (10), the $F_n^{\text{rec}}[\hat{\mathbf{\Omega}}_v^{(k)}]$ scalar term takes into account the antenna pattern in the receiving segment (this term suppresses all photons scattered to the radar receiver from outside the field of view). Term $\mathbf{P}_{\text{prop}}[\mathbf{r}_{\text{scat}}^{(k)} \to \mathbf{r}_{\text{rec}}]$ is the 4×4 propagation matrix that accounts for the extinction of the signal scattered back to the radar receiver. When propagating in nonisotropic media, this propagation matrix will induce polarization effects as well (see section 5.3 in Battaglia and Mantovani 2005). When the

photon intensity become smaller than a certain threshold, the tracing is terminated and a new photon is launched. By summing up over N_T photons and over the different orders of scattering, the algorithm provides an estimate of the mean apparent intensity received by the radar from range r as

$$\langle \bar{\mathbf{I}}_a(r) \rangle = \frac{1}{N_T} \sum_{j=1}^{N_T} \sum_{k=1}^{N_s} \bar{\mathbf{I}}_a^{(k)}(r)(j) \equiv \sum_{k=1}^{N_s} \bar{\mathbf{I}}_a^{(k)}(r), \qquad (11)$$

with N_s being the maximum scattering order. When using $N_s = 1$, only SS effects are taken into account.

Equation (11) represents the statistical MC equivalent of the nondimensional term inside the brackets on the right side of Eq. (8), with the only difference being that it includes the four Stokes components. When the radar emits a horizontal wave and the horizontal (vertical) component is considered in the receiving segment, the copolar reflectivity Z_{hh}^{MS} (the cross-polar reflectivity Z_{hv}^{MS}) will be computed by inserting Eq. (10) in Eq. (8). Therefore, parameters such as $Z_{\text{dr}}^{\text{MS}}$ and linear depolarization ratio $\text{LDR}_{vh}^{\text{MS}}$ are easily derived in the MC simulation as well. Although in this study we consider only isotropic media, because of MS effects cross-polar reflectivity signals can also of interest, as will be shown in section 5d.

4. Validation of the code

a. Single-scattering results

To validate the MC procedure, a very simple five-layer raining atmosphere is used. The five layers are each 1 km thick and contain raindrops with an exponential hydrometeor size distribution with fixed intercept as in the Marshall–Palmer size distribution (Marshall and Palmer 1948) and equivalent water contents equal to 0.3, 1.0, 1.8, 2.0, and 2.5 g m^{-3}, with the intensity increasing downward. At 35.5 GHz, this configuration leads to equivalent reflectivities equal to 33.5, 40.5, 43.4, 43.9, and 45.0 dBZ and to attenuations equal to 1.2, 5.1, 9.8, 11.0, and 13.9 dB km^{-1}, respectively. From these values it is straightforward to reconstruct the SS pencil-beam apparent reflectivity profile by accounting for the two-way path attenuation. One detail worth mentioning concerns the attenuation contribution from the same range bin where the reflectivity is computed. In fact, although the reflectivity value is attributed to the center of a fixed range bin at a distance r, the attenuation is not that corresponding to the same distance: Eq. (4) is not exact. In contrast, suppose that the equivalent reflectivity factor is constant and equal to $Z_e(r)$ in the radar bin of thickness Δr; then we can write
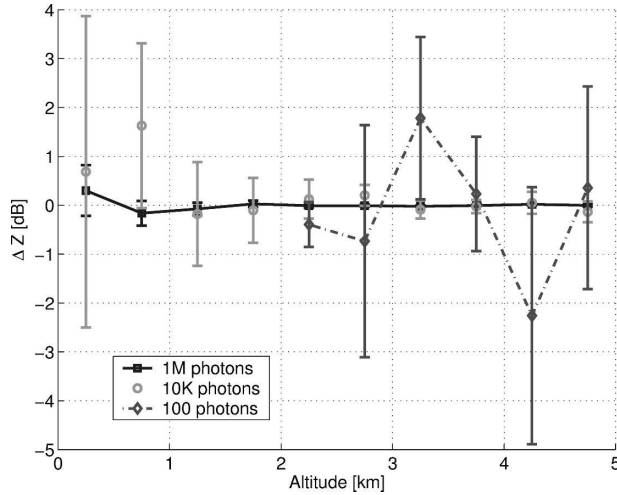
FIG. 2. Computed exact SS reflectivity for a 5-km-thick layer of rain (see text for details). The exact values of Z_a^{SS} are -28.6, -14.7, -3.8, 7.2, 16.9, 26.7, 30.6, 35.7, 31.7, and 32.9 dBZ for altitude between 0.25 and 4.75 km, with a step of 0.5 km. The radar vertical resolution and footprint diameter are 0.5 and 1 km, respectively. Different numbers of MC photons are used as indicated in the legend (1M = 10^6, 10K = 10^4). The error bars correspond to the 3-σ confidence level based on MC statistical noise.

$$Z_a(r) = Z_e(r)A_{2\text{-way}}(r - \Delta r/2) \frac{\int_0^{\Delta r} e^{-2k_{\text{ext}}z}\, dz}{\Delta r}$$

$$= Z_e(r)A_{2\text{-way}}(r - \Delta r/2) \frac{1 - e^{-2\tau}}{2\tau}, \qquad (12)$$

with k_{ext} and $\tau_{r \to r+\Delta r} = k_{\text{ext}}\Delta r$ being the extinction coefficient and the optical thickness of the bin, respectively. When passing to logarithmic values, Eq. (12) provides an attenuation factor (dB) equal to

$$A_{2\text{-way}}(r) = 2 \times 4.343\tau_{0 \to r - \Delta r/2}$$

$$+ 10 \log_{10}\left[\frac{1 - \exp(-2\tau_{r \to r+\Delta r})}{2\tau_{r \to r+\Delta r}}\right]. \qquad (13)$$

Note that only in the limit of small $\tau_{r \to r+\Delta r}$, $[1 - \exp(-2\tau_{r \to r+\Delta r})]/2\tau_{r \to r+\Delta r} \to \exp(-\tau_{r \to r+\Delta r})$ so that $A_{2\text{-way}}(r) \to 2 \times 4.343(\tau_{0 \to r - \Delta r/2} + 0.5\tau_{r \to r+\Delta r})$ and the attenuation can be computed as the two-way attenuation relative to the center of the bin $2 \times 4.343\tau_{0 \to r}$.

Figure 2 shows the departure from the exact analytical solution for Z_a^{SS} in the case of a spaceborne radar with a vertical resolution of 500 m and a footprint diameter of 1 km. To give an idea of the accuracy of the computations performed with the MC technique, in Fig. 2 the MC simulations have been performed for three different numbers of photons: 10^2, 10^4, and 10^6. Even in the presence of a strong attenuating profile one million

photons are enough to reach an accuracy of better than 0.2 dB in the whole profile. The accuracy obviously deteriorates going deeper inside the cloud because of the reduced number of photons that successfully reach the deepest layers. In the extreme case when $N_T = 100$, no photon is able to reach the layer below 2 km. In fact, the optical thickness above this layer is approximately equal to 5 so that, on average, only $N_T \exp(-5) \approx 0.6\%$ of N_T photons reach that layer. This is the reason why the dashed-diamond line stops at 2.25-km altitude in Fig. 2. Based on the MC statistics of each range bin (which will depend on the selected Δr), the code internally computes the variance of $\langle \bar{\mathbf{I}}_a(r) \rangle$ defined in Eq. (11) for each range bin. This can be converted to an error (related to the MC noise) for each of the analyzed radar quantities. In Fig. 2, results for each simulation are plotted with a corresponding error bar that represents the 3-σ confidence level based on MC statistical noise.

b. Relative importance of the contribution from the second order of scattering

As a test, the importance of the second order of scattering (relative to the first order) has been evaluated in a homogeneous layer having constant extinction and SS albedo and a generic phase function $p(\Theta)$ [normalized by the condition $\int_{-1}^{1} p(\Theta)\, d\cos(\Theta) = 2$]. Note that Θ is the scattering angle, that is, the angle between the incident and the scattered direction. We expect that the second order of scattering becomes more relevant with deeper penetration into the layer; this contribution should also increase linearly with the SS albedo. For illustration, consider Fig. 3 in which the nadir downlooking radar is positioned at an altitude H_{radar} above the homogeneous layer (at the point F_1). Here we consider a monostatic radar, the antenna pattern of which is pencil-beam-like in the emitting segment and Gaussian in the receiving segment. At depths between z and $z + \Delta z$, the second-order-of-scattering effect results from an integral over all possible second order-of-scattering contributions by photons interacting the first time at P_1 and the second time at P_2. Note that P_2 has to be located between the two spheroids with the same foci F_1 and F_2 (located at the radar position and in P_1) and with the rotational symmetry axis length equal to $2a_1 = 2z - z_1 + H_{\text{rad}}$ and $2a_2 = 2(z + \Delta z) - z_1 + H_{\text{rad}}$. In fact, by using the ellipse definition property, the path undergone by the photons emitted by the radar, scattered in P_1 and then scattered back to the radar in P_2, is between $H_{\text{rad}} + z_1 + 2a_1$ and $H_{\text{rad}} + z_1 + 2a_2$, corresponding to an apparent range between $H_{\text{rad}} + z$ and $H_{\text{rad}} + z + \Delta z$. The probability of a photon being scattered at a penetration depth between z_1 and $z_1 + dz_1$,
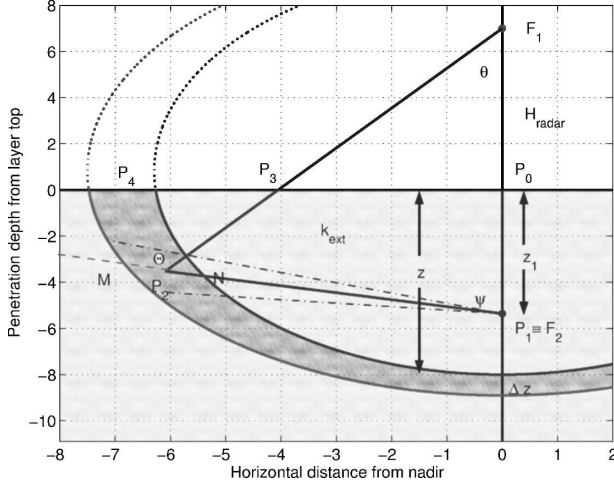
FIG. 3. Schematic for the evaluation of the relative magnitude of the second-order-of-scattering contribution. For explanations see text.
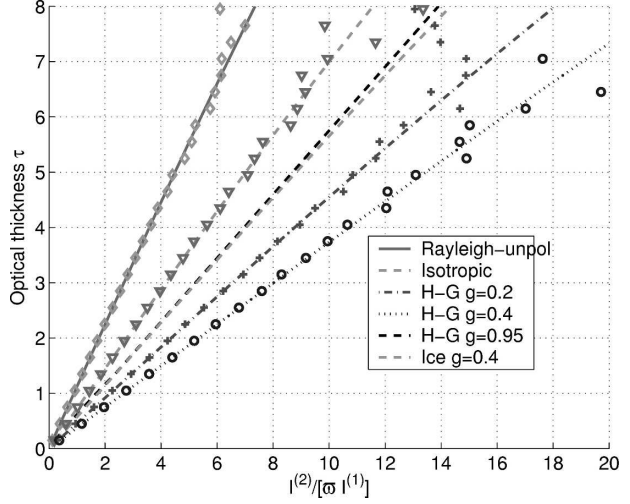

FIG. 4. Evaluation of the magnitude of the second order of scattering as a function of the traveled optical thickness for a uniform layer with different phase functions. The results corresponding to an H–G phase function with $g = 0.95$ are almost indistinguishable from those obtained with a Mie phase function with $g = 0.4$. Results are computed with no antenna suppression factor: lines are the analytical solutions, and symbols are the MC results.

$dP(z_1)$, is proportional to the SS albedo ϖ and, according to Beer–Lambert–Bouguer law, to the factor k_{ext} $\exp(-k_{ext}z_1)dz_1$, that is,

$$dP(z_1) = \varpi k_{ext}e^{-k_{ext}z_1}dz_1. \qquad (14)$$

The fraction of photons being scattered in the ellipsoidal segment with polar angles between ψ and $\psi + d\psi$ will be

$$d\mathcal{F}(\psi) = \varpi k_{ext}\Delta r(\psi)e^{-k_{ext}r(\psi)}\frac{p(\psi)}{2}d\cos\psi, \qquad (15)$$

with $r(\psi) = \overline{P_1P_2}$ and $\Delta r(\psi) = \overline{MN}$ (see Fig. 3 for definition of points M and N). This fraction of photons, when going back to the radar, undergoes a path attenuation equal to $\exp(-k_{ext}\Delta\xi)$, with $\Delta\xi = \overline{P_1P_2} + \overline{P_2P_3}$ and an antenna attenuation corresponding to the angle θ; the scattering angle is given by $\Theta_{sca} = \theta + \psi$ so that a correction factor equal to $p(\Theta_{sca})/(4\pi)$ also has to be included. Note that the photon scattered both at P_1 and P_2 is always less attenuated than the SS photons with the same apparent range gate. The medium path difference is equal to $\overline{F_1P_3} - \overline{F_1P_0}$, and it increases with θ.

Therefore, using azimuthal symmetry, the total fraction of photons first scattered at P_1 and then at any point will be

$$\Delta\mathcal{F}(z_1) = \int_{\psi_1}^{\pi} e^{-k_{ext}\Delta\xi(\psi)}e^{-4\log^2\left(\frac{\theta_v}{\eta_{3dB}}\right)^2}\frac{p(\Theta_{sca})}{4\pi}d\mathcal{F}(\psi). \qquad (16)$$

Thus, the fraction of photons backscattered twice with an apparent range between z and $z + \Delta z$ will be

$$\mathcal{F}[z, (2)] = \int_0^z \Delta\mathcal{F}(z_1)dP(z_1). \qquad (17)$$

On the other hand, the fraction of photons being backscattered only once and with apparent range between z and $z + \Delta z$ will undergo an additional z-long path inside the attenuating medium (but no antenna suppression), so that

$$\mathcal{F}[z, (1)] = \varpi k_{ext}\Delta z e^{-k_{ext}z}\frac{p(\pi)}{4\pi}e^{-k_{ext}z}, \qquad (18)$$

where p denotes the phase function. The fraction of photons backscattered twice divided by the fraction backscattered once, that is, the ratio obtained by dividing Eq. (17) by Eq. (18), provides a way to assess the magnitude of the second order of scattering relative to the first order. As a first obvious consideration, this ratio has a dependence on ϖ, and the higher the SS albedo is, the higher is the effect.

The analytical model has been exploited to validate the second-order-of-scattering results as computed with the MC method. Figure 4 shows the ratio $\mathcal{F}[z, (2)]/\{\varpi\mathcal{F}[z, (1)]\}$ evaluated for different phase functions when considering an infinite-aperture antenna (so no antenna suppression factor is present). Figure 4 shows an almost perfect agreement between the analytical (line style) and the MC (symbol style) results. The disagreement at optical thickness higher than 5 is due to

MC noise that becomes relevant at high optical thicknesses. In this case, the impact of the second order of scattering depends only on the optical thickness τ traveled inside the medium: the higher the optical thickness is, the higher is the MS effect. As an example (see Fig. 4), in an isotropic medium with an albedo equal to 0.1 the second order of scattering has almost the same magnitude as the SS at an optical thickness of 7 whereas in a Rayleigh medium with the same albedo it is almost one-half as much at an optical thickness of 6. To evaluate the effect of the increased forward scattering for higher microwave frequencies, different phase functions have been used in Fig. 4. In particular, we have included a Rayleigh (for unpolarized radiation), an isotropic, and a Heyney–Greenstein (H–G) phase function with different g parameters. For comparison purposes, and because of the difference between this and realistic phase functions in the backscattering region, we have included a phase function for a distribution of spherical ice crystals with the same $g = 0.4$. The simulations show that an increase in g causes first an increase in the MS contribution and then a decrease with the turning point for g around 0.5. For instance, at an optical thickness of 3 and a phase function with $g = 0.2$, 0.4, and 0.95, the corresponding magnitude of the second order of scattering is 1.57, 1.92, and 1.25 times the value of the corresponding isotropic phase function. In fact, as g increases, more photons contribute to the integration in Eq. (16) because photons that are scattered with scattering angle higher than $\pi - \psi_1$ (with $\psi_1 = \widehat{F_1 P_1 P_4}$) do not contribute to the integral in Eq. (16). At a certain point at which practically all radiation is scattered in P_1 with scattering angles lower than $\pi - \psi_1$, a further increase in g actually has a negative effect in terms of the magnitude of the second order of scattering. In effect, the scattering phase function $p(\Theta_{sca})$ [which also enters the integral Eq. (16)] decreases monotonically with Θ_{sca} (and in particular has a minimum at $\Theta_{sca} = \pi$). When the scattering at P_1 is mainly in the forward direction, the scattering angles in P_2 will be primarily close to π. The opposite behavior occurs when the scattering at P_1 distributes photons in all the shaded area in Fig. 3, when scattering angles as large as $\pi/2$ are allowed to happen in P_2. The balance between the two effects decreases the ratio $\mathcal{F}[z, (2)]/\{\varpi \ \mathcal{F}[z, (1)]\}$ for high g ($g \geq 0.5$) for the H–G-like phase functions. This turning point for the g value will move to higher values when the antenna pattern is considered. In this case, the effective area to be considered will be the intersection between the shaded area of Fig. 3 and the antenna pattern. In the hypothetical case of a phase function that scatters radiation only in the forward direction (and just allowing for a small fraction to be backscattered), we can actually forecast the ratio $\mathcal{F}[z, (2)]/\{\varpi \ \mathcal{F}[z, (1)]\}$ to be equal to the optical thickness τ itself. In this case, the photons scattered twice are simply those that make the same exact path as the photons scattered once. Another factor should be taken into consideration: with more forward scattering, the differential attenuation between the first-order-scattered and second-order-scattered photons (which favors the second-order contribution) is less pronounced. However, this effect can be neglected when considering spaceborne configurations (for which the difference $\overline{F_1 P_3} - \overline{F_1 P_0}$ is typically negligible).

Note that in Fig. 4, because of the different slopes, the Rayleigh phase function has less MS than the isotropic one—this is mainly due to the fact that the backscattering ratio $p(\Theta_{sca})/p(\pi)$ is generally lower and because more photons are "lost" when scattered at scattering angles higher than $\pi - \psi_1$. The result labeled as "Rayleigh unpol" ("Rayleigh pol") (see Fig. 7, described in section 5b), represents the scalar (vector) solution of the radiative transfer equation (but in both cases with unpolarized impinging radiation). When polarization is considered, the Rayleigh results are closer to the isotropic results. In a similar way, the real phase function gives less MS effect relative to that of the H–G with the same g; because of the backscattering peak of the real phase function, the backscattering ratio is typically lower in this case.

For an infinite antenna beamwidth (see Fig. 4), the MS tends to increase almost linearly with the optical thickness: in fact, no antenna factor suppresses the contributions from regions far away from the radar zenith foot. When the beamwidth is considered (Fig. 5), the increase with the optical thickness is strongly damped. When k_{ext} becomes sufficiently high, the antenna pattern is no longer important and the results tend to be equal to those for an infinite-beamwidth-antenna pattern (reproduced in Fig. 5 and indicated as $k_{ext} = \infty$ in the legend). Moreover, at the same τ, the effect is larger for media with higher k_{ext} because the antenna factor suppresses all contributions from regions far from nadir. The difference between the dotted lines and the other lines practically accounts for the departures between taking into account the antenna pattern or working in the 1D assumption like Marzano et al. (2003) (which generally overestimates the effect). As before, very good agreement between the MC results and the analytical model can be seen by comparing the symbols and line-style curves in Fig. 5.
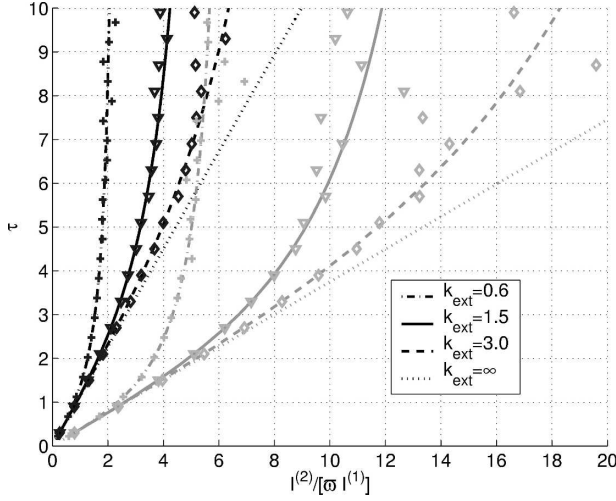
FIG. 5. Same as Fig. 4, but including the effect of the antenna pattern. A uniform layer with different phase functions (black lines for unpolarized Rayleigh; gray lines for H–G with $g = 0.4$) and extinction coefficients (as indicated in the legend; km^{-1}) is considered. The results are evaluated with an antenna pattern with a horizontal resolution of 5.2×5.2 km^2. The curves labeled by $k_{ext} = \infty$ correspond to no antenna-pattern suppression factor (so they reproduce the corresponding results of Fig. 4). Lines correspond to the analytical solutions; symbols correspond to the MC results.

5. Evaluation of MS effects for a homogeneous layer

The MC code has been used to understand which of the scattering properties are most relevant when considering the MS signal. For this purpose, the MS effect is evaluated for a single-layer atmosphere characterized by fixing an SS albedo ϖ and a phase function and varying the extinction coefficient k_{ext} independently.

It is useful to introduce the "scattering optical thickness," defined as the integral over distance of the scattering coefficient (i.e., particle density times scattering cross sections):

$$\varpi\tau(z) \equiv \int_{H_{top}}^{z} k_{ext}\varpi\, dz, \qquad (19)$$

where H_{top} indicates the altitude of the top of the medium.

a. Magnitude of the successive orders of scattering

The MC code records the contribution of each order of scattering $I_a^{(k)}(r)$ to the total signal $I_a(r)$ [see Eq. (11)]. In particular, it is possible to evaluate the magnitude of the successive orders of scattering by computing the ratio $f(k) = I_a^{(k)}(r)/I_a(r)$. Figure 6 shows the magnitude of different orders of scattering when going
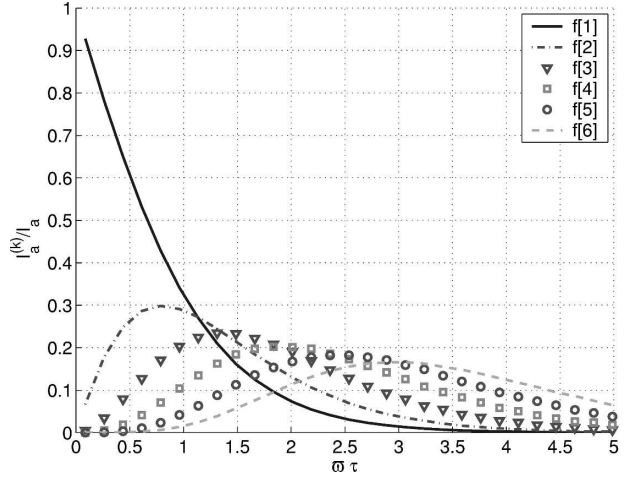

FIG. 6. Evaluation of the magnitude of the k order of scattering $f(k)$ as a function of the traveled scattering optical thickness for a uniform layer with an unpolarized Rayleigh phase function. No antenna suppression factor is considered.

inside the medium for an unpolarized Rayleigh phase function. The incoming radiation is collimated at nadir, and no antenna pattern suppression factor is considered in the receiving segment. The radar vertical resolution is selected to be so small ($\Delta r = 50$ m) that $k_{ext}\Delta r \ll 1$; in other words, the radar pulse (multiplied by 0.5 times the speed of light) is much shorter than the mean free path. If this condition is not fulfilled, the scaling properties with the scattering optical thickness no longer hold. At ranges within which the scattering optical thickness is equal to 1, the contributions of the first and second orders of scattering to the radar signal are approximately 30%, whereas the third and the fourth orders of scattering contribute approximately 20% and 10%, respectively. It is obvious that the contributions from higher scattering orders increase with the scattering optical thickness. Figure 6 indicates that the peak contribution of each scattering order decreases with scattering order while the scattering optical depth associated with the peak contribution of each scattering order increases with scattering order. Note that the results plotted in Fig. 6 correspond to an albedo $\varpi = 0.5$, but identical results have been found for other albedos. Therefore, at the same scattering optical depth, the result is independent of the values assumed for the albedo and the extinction coefficient of the medium but depends only on the product of the two. For the second order of scattering, this can be understood by looking at the integral in Eq. (17): when spaceborne configurations are considered, the product of the three terms $\exp[-k_{ext}\Delta\xi(\psi)]$, $\exp[-k_{ext}r(\psi)]$, and $\exp(-k_{ext}z_1)$ can be taken out of the integral because it is practically equal to $\exp(-2k_{ext}z)$. Therefore, Eq. (17) becomes
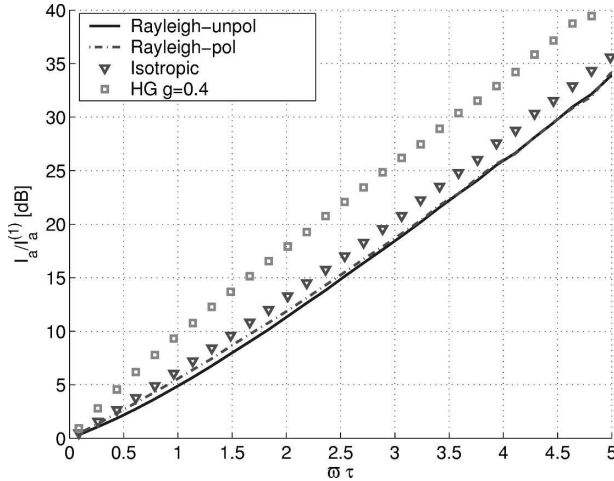
FIG. 7. Ratio between the total signal and the first-order-of-scattering contribution as a function of the scattering optical thickness for different phase functions (as indicated in the legend). No antenna suppression factor is considered.
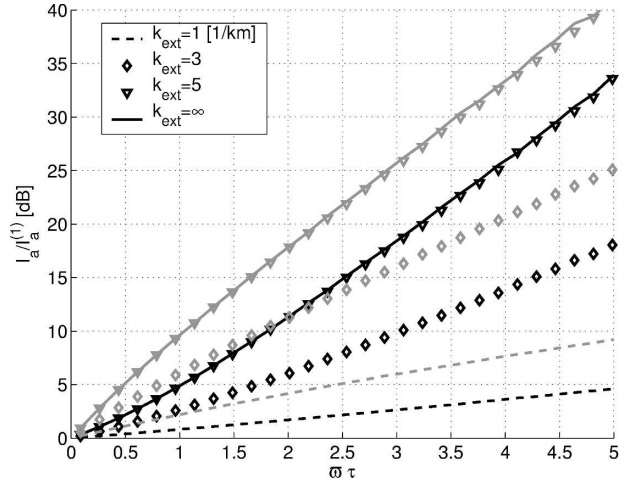
FIG. 8. Ratio between the total signal and the first order of scattering as a function of the scattering optical thickness for the Rayleigh unpolarized (black lines) and for the H–G with $g = 0.4$ (gray lines) phase function. Media with different extinction coefficients are considered, and an antenna pattern with a horizontal resolution of 5.2×5.2 km^2 is applied in the receiving antenna.

$$\mathcal{F}[z, (2)] = (\varpi k_{\text{ext}})^2 e^{-2k_{\text{ext}}z} \mathcal{H}^{(2)}(z), \qquad (20)$$

where $\mathcal{H}^{(2)}$ is related to the phase function of the medium and the radar bin width Δz only. The same kind of argument can essentially be used for the successive order of scattering, except that the geometry is not as simple. Because at order (n) it is expected that

$$\mathcal{F}[z, (n)] = (\varpi k_{\text{ext}})^n e^{-2k_{\text{ext}}z} \mathcal{H}^{(n)}(z), \qquad (21)$$

in the relative contributions of the different orders of scattering $f(k)$ the term $\exp(-2k_{\text{ext}}z)$ will cancel out (and with it the dependence on k_{ext}). The same results are therefore found for equal ϖk_{ext} values. Slightly different curves are found when different phase functions are used. This invariance property fails when the antenna suppression factor $\exp[-4 \log 2(\theta_\nu/\eta_{3\text{dB}})^2]$ is taken into account.

b. Relative weight between single scattering and total signal

For radar computations, it is relevant to evaluate the magnitude of the first order of scattering relative to that of the total signal. Figure 7 shows the total signal versus the SS signal (in decibel scale, i.e., 10 times the logarithm in base 10 of the quantity) for different phase functions. Because no antenna pattern is considered, these values can be considered as the highest reachable for a given scattering optical thickness. For a medium with H–G with $g = 0.4$ or a Rayleigh phase function and a scattering optical depth of 2, the total signal I_a can be 18 and 11.4 dB higher than the SS signal $I_a^{(1)}$, respectively. These results reflect the method employed by

Marzano et al. (2003). However, when an antenna pattern configuration like that envisaged for the GPM satellite is taken into account, the results are very different, as shown in Fig. 8. The antenna pattern strongly reduces the MS effect when media with smaller extinction coefficient (i.e., higher mean free path) are considered. In the limit $k_{\text{ext}} \to 0$ the antenna factor does not play any role, whereas for $k_{\text{ext}} \to \infty$ the antenna pattern completely suppresses the MS effect. As shown in Fig. 8, with a horizontal resolution footprint on the order of 5 km, the antenna effect is negligible for media for which the extinction coefficient is higher than 5 km^{-1}. However, these values are never exceeded when real hydrometeors are considered for frequencies below 35 GHz (see Part II). A fortiori, the antenna pattern plays a major role even when airborne configurations are considered.

c. Evaluation of the damping distance for single-layered cloud

The MS contribution has another important feature: when single-layer cloud structures are present, the cloud appears thicker to the radar than it really is. In Fig. 9 the MS and the SS reflectivities for a single uniform layer with a scattering optical depth equal to 1, with an optical depth equal to 2, and with different extinction coefficients (and with clear air underneath) are shown. The figure compares favorably to Fig. 2 in Ito et al. (1995). A polarized Rayleigh phase function is considered. The SS reflectivities are different for dif-
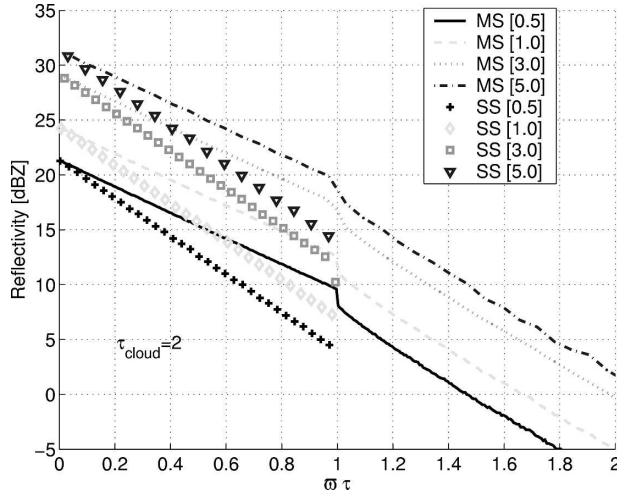
FIG. 9. The MS and SS signal from layers with different extinction coefficients but with the same scattering optical thickness. An SS albedo ϖ equal to 0.5 and a Rayleigh-polarized phase function are considered. In the legend, the values in brackets represent the different extinction coefficients of the layer (km^{-1}).

FIG. 10. LDR$_{hv}$ as a function of the scattering optical depth for three different phase functions as indicated in the legend. No antenna suppression factor is considered here. For the computation performed with the Mie phase function with $g = 0.7$, the MC noise is illustrated by error bars. In this case, 2×10^6 photons have been used.

ferent k_{ext} (more extinguishing Rayleigh media have higher backscattering). Here, Z_a^{SS} decays inside the layer; attenuation (dB) is equal to 8.6859τ at an optical depth equal to τ. When the boundary of the cloud is reached at $\varpi\tau = 1$, the SS reflectivities abruptly vanish; in contrast, the MS reflectivity decreases gradually, indicating the loss of the SS contribution, but remains significant below the lower boundary of the cloud. To have an idea about how far this signal can go in the region below the cloud, we can introduce a decay thickness $d_{\downarrow 10dB}$, defined as the depth that has to be traveled inside the clear-air region below the cloud so that the reflectivity could decay by 10 dB (from the MS reflectivity value sensed at the bottom of the cloud). As an example, the cloud with $k_{ext} = 0.5$ km^{-1} has a reflectivity at the rear-cloud-edge altitude equal to $Z_a^{MS} = 10$ dBZ. The apparent reflectivity Z_a^{MS} decays to 0 dBZ only at $\varpi\tau = 1.45$, so that $d_{\downarrow 10dB} = 0.45/(0.5 \times 0.5) = 1.8$ km. Note that in Fig. 9 the clear region has no additional scattering optical depth: the values plotted along the x axis at scattering optical depths greater than 1 are an extrapolation at larger ranges based on the SS albedo and the extinction coefficient of the cloud itself.

When no antenna is accounted for, results are almost independent of the SS albedo and the extinction of the layer; in rough terms, the MS is strongly damped in less than one-half of the thickness of the layer. The $d_{\downarrow 10dB}$ values obtained when a realistic spaceborne configuration is taken into account are lower than the previous ones, as expected, and this reduction is more pronounced with low extinction coefficients. In particular,
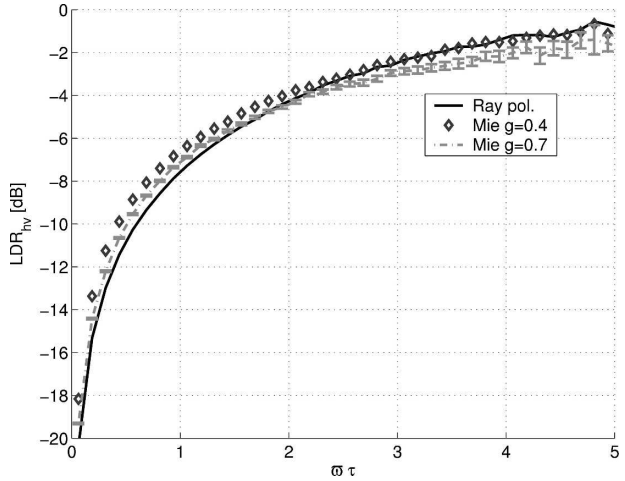
this excludes the possibilities of second trip echoes. In fact, with current pulse repetition frequencies of spaceborne radars (on the order of 2500–5000 Hz) the distance between successive pulses is on the order of 120–60 km—that is, far higher than a typical thickness of a cloud. We thus can infer that MS cannot produce echoes seen by the next pulse.

d. Evaluation of LDR signals

Another important MS effect is the presence of strong cross-polarized components in the received radar signal. The linear depolarization ratio LDR$_{vh}^{MS} \equiv Z_{vh}^{MS}/Z_{hh}^{MS}$ has been evaluated for a homogeneous layer characterized by different phase functions. Figure 10 presents the results of the simulation performed with no antenna pattern suppression. A polarized Rayleigh and two Mie phase functions (with asymmetry parameters equal to 0.4 and 0.7, respectively) are considered. As before, the results scale up with the scattering optical depth, with the LDR signal monotonically increasing with this quantity [a result already known in the lidar counterpart; e.g., Sassen and Zhao (1995); Hu et al. (2001)]. At small scattering optical depths, more-forward-peaked phase functions cause larger LDRs, but the reverse is true at scattering optical depth greater than 2. However, for asymmetry factors lower than 0.4, as are commonly found at GPM frequencies, and at scattering optical depth greater than 2, the results tend to be almost independent of the phase function. Note how very high values close to 0 dB can be

found at large scattering optical depth (>5), a signature that will be particularly relevant in Part II of this series. Again, when the antenna pattern is considered, the magnitude of LDR can be strongly reduced. The results do not scale up with the scattering optical depth any more: at the same $\varpi\tau$, homogeneous layers with small SS albedos and extinction coefficients produce LDR signals that are smaller than in the layers characterized by high SS albedos and extinction coefficients.

6. Discussion and conclusions

A numerical code based on an MC procedure that is capable of simulating the polarized signal of a (monostatic/bistatic) radar as sensed from nonisotropic media has been described and validated. The method is not able to account for backscattering enhancement. However, this effect has been shown to be negligible (Kobayashi et al. 2005) in the spaceborne systems that are the foci of this work. The code has been exploited to have insight into the MS phenomenon by using a uniform layer as a case study. The magnitude of the SS with respect to the total radar return (see Fig. 7) is primarily a function of the scattering optical depth [defined in Eq. (19)], with the MS effect increasing with the traveled scattering optical depth. When the antenna suppression factor is omitted, results in spaceborne configuration are found to depend only on the product ϖk_{ext}. The asymmetry parameter of the phase function also plays an important role, with MS contributions increasing when passing from the Rayleigh phase function to the phase function with g values around 0.4 (see Fig. 4). Realistic asymmetry factors do not exceed this value at GPM frequencies (see Part II).

Similar to the results of Kobayashi et al. (2004, 2005), the Battaglia et al. (2005a) study also shows that, at scattering optical depth greater than 2, antenna pattern plays a key role in reducing the MS contributions. In essence, what really matters is the interplay among the radiation mean free path, the radar footprint (and thus the product of the satellite altitude and the tangent of the beamwidth), the scattering-layer SS albedo coefficient, and the distance traveled inside the medium. The importance of MS effects increases with the depth traveled, with the SS albedo of the scattering medium (which enhances the probability of scattering events vs absorption events), and for mean free paths that are much lower than the horizontal resolution. When GPM footprints are considered, the MS effects are certainly reduced to those values obtained for an infinite-beamwidth-like antenna for extinction coefficients on the order of 5 km^{-1}. When less extinguishing media are considered, however, the suppression by the antenna pattern can be substantial (see Fig. 8). Therefore, the

approach used by Oguchi et al. (1994) and Marzano et al. (2003) generally overestimates the MS effects when typical spaceborne radar conditions are met, because they effectively assume plane-wave incidence. Their solution can a fortiori only exclude the presence of MS when absent but cannot be used to assess the effective amount of the MS contributions. This factor is even more critical when airborne configurations are examined. In agreement with results already present by Ito et al. (1995), section 5c reveals that MS effects can be responsible for overestimation in the detection of cloud bottom boundaries, and section 5d shows that MS enhances the cross-polarized component. This is believed to be a key signature of MS effects.

In Part II, the MC numerical model presented here serves as the basis for simulating the SS and MS radar return at the GPM frequencies for different inhomogeneous hydrometeor profiles extracted from some cloud-resolving-model simulations.

REFERENCES

Battaglia, A., and S. Mantovani, 2005: Forward Montecarlo computations of fully polarized microwave radiation in non isotropic media. *J. Quant. Spectrosc. Radiat. Transfer,* **95,** 285–308.

——, M. O. Ajewole, and C. Simmer, 2005a: Multiple scattering effects due to hydrometeors on precipitation radar systems. *Geophys. Res. Lett.,* **32,** L19801, doi:10.1029/2005GL023810.

——, and Coauthors, 2005b: Emission and scattering by clouds and precipitation. *Thermal Microwave Radiation: Applications for Remote Sensing,* C. Mätzler, Ed., IET Electromagnetic Waves Series 52, Institution of Engineering and Technology, 101–223.

——, M. O. Ajewole, and C. Simmer, 2006: Evaluation of radar multiple-scattering effects from a GPM perspective. Part II: Model results. *J. Appl. Meteor. Climatol.,* **45,** 1648–1664.

Bissonnette, L. R., 1996: Multiple-scattering lidar equation. *Appl. Opt.,* **35,** 6449–6465.

——, and Coauthors, 1995: Lidar multiple scattering from clouds. *Appl. Phys.,* **60B,** 355–362.

Bringi, V. N., and V. Chandrasekar, 2001: *Polarimetric Doppler Weather Radar, Principles and Applications.* Cambridge University Press, 636 pp.

Doviak, R. J., and D. S. Zrnić, 1984: *Doppler Radar and Weather Observations.* Academic Press, 562 pp.

Ferrauto, G., F. Marzano, and G. Vulpiani, 2004: Model-based sensitivity analysis of incoherent effects on microwave radar observations of precipitation media. *Proc. of ERAD 2004,* Visby, Sweden, Copernicus GmbH, 428–434.

Gasiewski, A., 1993: Microwave radiative transfer in hydromete-

ors. *Atmospheric Remote Sensing by Microwave Radiometry,* M. A. Janssen, Ed., John Wiley and Sons, 91–144.

House, L., and L. W. Avery, 1969: The Monte Carlo technique applied to radiative transfer. *J. Quant. Spectrosc. Radiat. Transfer,* **9,** 1579–1591.

Hu, Y.-X., D. Winkler, P. Yang, B. Baum, L. Poole, and L. Vann, 2001: Identification of cloud phase from PICASSO-CENA lidar depolarization: A multiple scattering sensitivity study. *J. Quant. Spectrosc. Radiat. Transfer,* **70** (4–6), 569–579.

Hubbert, J., and V. N. Bringi, 2000: The effects of three-body scattering on differential reflectivity signatures. *J. Atmos. Oceanic Technol.,* **17,** 51–61.

Iguchi, T., T. Kozu, R. Meneghini, J. Awaka, and K. Okamoto, 2000: Rain-profiling algorithm for the TRMM precipitation radar. *J. Appl. Meteor.,* **39,** 2038–2052.

Ito, S., T. Oguchi, T. Iguchi, H. Kumagai, and R. Meneghini, 1995: Depolarization of radar signals due to multiple scattering in rain. *IEEE Trans. Geosci. Remote Sens.,* **33,** 1057–1062.

Kobayashi, S., S. Tanelli, T. Iguchi, and E. Im, 2004: Backscattering enhancement with a finite beam width for millimeter-wavelength weather radars. *Microwave Remote Sensing of the Atmosphere and Environment IV,* G. S. Jackson and S. Uratsuka, Eds., International Society for Optical Engineering (SPIE Proceedings Vol. 5654), 106–113.

——, ——, and E. Im, 2005: Second-order multiple-scattering theory associated with backscattering enhancement for a millimeter wavelength weather radar with a finite beam width. *Radio Sci.,* **40,** RS6015, doi:10.1029/2004RS003219.

Kozu, T., and Coauthors, 2001: Development of precipitation radar onboard the Tropical Rainfall Measuring Mission satellite. *IEEE Geosci. Remote Sens.,* **39,** 102–116.

Kummerow, C. D., W. Barnes, T. Kozu, J. Shiue, and J. Simpson, 1998: The Tropical Rainfall Measuring Mission (TRMM) sensor package. *J. Atmos. Oceanic Technol.,* **15,** 809–817.

Marshall, J. S., and W. M. Palmer, 1948: The distribution of raindrop with size. *J. Meteor.,* **5,** 165–166.

Marzano, F. S., L. Roberti, S. Di Michele, A. Mugnai, and A. Tassa, 2003: Modeling of apparent radar reflectivity due to convective clouds at attenuating wavelengths. *Radio Sci.,* **38,** 1002, doi:10.1029/2002RS002613.

Marzoug, M., and P. Amayenc, 1994: A class of single- and dual-frequency algorithms for rain-rate profiling from a space-borne radar. Part I: Principle and tests from numerical simulations. *J. Atmos. Oceanic Technol.,* **11,** 1480–1506.

Mishchenko, M. I., J. W. Hovenier, and L. D. Travis, Eds., 2000: *Light Scattering by Non-spherical Particles.* Academic Press, 690 pp.

Mugnai, A., 2003: Contribution to the global precipitation measurements by the proposed European GPM (EGPM) satellite. *Geophys. Res. Abstracts,* **5,** 12 470.

Oguchi, T., N. Ishida, and T. Ihara, 1994: Effect of multiple scattering on the estimation of rainfall rates using dual-wavelength radar techniques. *IEEE Trans. Geosci. Remote Sens.,* **32,** 943–946.

Olson, W. S., P. Bauer, N. R. Viltard, D. E. Johnson, W. Tao, R. Meneghini, and L. Liao, 2001: A melting layer model for passive/active microwave remote sensing applications. Part I: Model formulation and comparison with observations. *J. Appl. Meteor.,* **40,** 1145–1163.

Roberti, L., and C. Kummerow, 1999: Monte Carlo calculations of polarized microwave radiation emerging from cloud structures. *J. Geophys. Res.,* **104,** 2093–2104.

Sassen, K., and H. Zhao, 1995: Lidar multiple scattering in water droplet clouds: Toward an improved treatment. *Opt. Rev.,* **2,** 394–400.

Stephens, G. L., and Coauthors, 2002: The CLOUDSAT mission and the A-train. *Bull. Amer. Meteor. Soc.,* **83,** 1771–1790.

Testud, J., P. Amayenc, and M. Marzoug, 1992: Rainfall-rate retrieval from a spaceborne radar: Comparison between single-frequency, dual-frequency, and dual-beam techniques. *J. Atmos. Oceanic Technol.,* **9,** 599–623.

Tsang, L., J. A. Kong, and R. T. Shin, 1985: *Theory of Microwave Remote Sensing.* Wiley-Interscience, 613 pp.